

CROSS-CORRELATION OF NEAR AND FAR-INFRARED BACKGROUND ANISOTROPIES AS TRACED BY
SPITZER AND *HERSCHEL*CAMERON THACKER¹, YAN GONG¹, ASANTHA COORAY¹, FRANCESCO DE BERNARDIS², JOSEPH SMIDT³, KETRON MITCHELL-WYNNE¹¹Department of Physics and Astronomy, University of California, Irvine, CA 92697 USA²Department of Physics, Cornell University, Ithaca, NY 14853 USA and³T-2, Los Alamos National Laboratory, Los Alamos, NM 87545 USA

Draft version March 1, 2024

ABSTRACT

We present the cross-correlation between the far-infrared background fluctuations as measured with the *Herschel* Space Observatory at 250, 350, and 500 μm and the near-infrared background fluctuations with *Spitzer* Space Telescope at 3.6 μm . The cross-correlation between far and near-IR background anisotropies are detected such that the correlation coefficient at a few to ten arcminute angular scales decreases from 0.3 to 0.1 when the far-IR wavelength increases from 250 μm to 500 μm . We model the cross-correlation using a halo model with three components: (a) far-IR bright or dusty star-forming galaxies below the masking depth in *Herschel* maps, (b) near-IR faint galaxies below the masking depth at 3.6 μm , and (c) intra-halo light, or diffuse stars in dark matter halos, that is likely dominating fluctuations at 3.6 μm . The model is able to reasonably reproduce the auto correlations at each of the far-IR wavelengths and at 3.6 μm and their corresponding cross-correlations. While the far and near-IR auto-correlations are dominated by faint dusty, starforming galaxies and intra-halo light, respectively, we find that roughly half of the cross-correlation between near and far-IR backgrounds is due to the same dusty galaxies that remain unmasked at 3.6 μm . The remaining signal in the cross-correlation is due to intra-halo light present in the same dark matter halos as those hosting the same faint and unmasked galaxies. In this model the decrease in the cross-correlation signal from 250 μm to 500 μm comes from the fact that the galaxies that are primarily contributing to 500 μm fluctuations peak at a higher redshift than those at 250 μm .

Subject headings: cosmology: observations – submillimeter: galaxies – infrared: galaxies – galaxies: evolution – cosmology: large-scale structure of Universe

1. INTRODUCTION

The cosmic infrared background (CIB) contains the total emission history of the Universe integrated along the line of sight. The CIB contains two peaks, one at optical/near-IR wavelengths around 1 μm and the second at far-IR wavelengths around 250 μm (Dole et al. 2006). The former is composed of photons produced during nucleosynthesis in stars while the latter is reprocessing of some of those photons by dust in the universe. While the total intensity in the near-IR background, especially at 3.6 μm , has been mostly resolved to individual galaxies, we are still far from directly resolving the total CIB intensity at 250 μm and above to individual sources. This is due to the fact that at far-IR wavelengths observations are strongly limited by the aperture sizes. With the SPIRE Instrument (Griffin et al. 2010) aboard the *Herschel* Space Observatory (Pillbratt et al. 2010)¹, the background has been resolved to 5%, 15% and 22% at 250 μm , 350 μm and 500 μm , respectively (Oliver et al. 2010). In order to understand some properties of the faint far-IR sources it is essential that we study the fluctuations or the anisotropies of the background.

These spatial fluctuations in the CIB are best studied using the angular power spectrum. This technique provides a way to study the faint and unre-

solved galaxies because while not individually detected, they trace the large scale structure. The clustering of these galaxies is then measurable through the angular power spectrum of the background intensity variations Amblard et al. (2011). Such fluctuation clustering measurements at far-IR wavelengths have been followed up with both *Herschel* and Planck (Viero et al. 2013; Planck Collaboration 2014), the latter of which has provided the highest signal to noise calculation in the far-IR.

Separately near-IR background anisotropies have been studied in the literature and have been interpreted as due to galaxies containing PopIII stars present during reionization (Kashlinsky et al. 2005, 2007, 2012), direct collapse black holes at $z > 12$ (Yue et al. 2013), and intra-halo light (Cooray et al. 2012; Zemcov et al. 2014). In addition to *Spitzer* at 3.6 μm and above, fluctuation measurements in the near-IR wavelengths have come from Akari (Matsumoto et al. 2011) and recently with the Cosmic Infrared Background Experiment (CIBER) at 1.1 and 1.6 μm (Zemcov et al. 2014). While earlier studies argued for a substantial contribution from galaxies at $z > 8$, including those with PopIII stars or blackholes, recent studies find that such signals are not likely to be the dominant contribution (Cooray et al. 2012; Yue et al. 2014). Both Cooray et al. (2012) using *Spitzer* and Zemcov et al. (2014) using CIBER argue for the case that the signal is coming from low redshifts and proposes an origin that may be associated with intra-halo light. Intra-halo light involves diffuse stars that are

¹ *Herschel* is an ESA space observatory with science instruments provided by European-led Principal Investigator consortia and with important participation from NASA.

tidally stripped during galaxy mergers and other interactions. However, we still expect some signal from galaxies during reionization. In addition to these two, there is also a third contribution. These are the faint, dwarf galaxies that are present between us and reionization. Such galaxies contribute to the near-IR and since they have flux densities below the point source detection level in near-IR maps, they remain unmasked during fluctuation power spectrum measurements. The exact relative amplitudes of each of these three signals are yet to be determined.

While fluctuations have been studied separately at far-IR and near-IR wavelengths, no attempt has been made to combine those measurements yet. In this work, we present the first results from just such a cross-correlation. We make use of the overlap coverage in the eight square degrees Boötes field between SDWFS at $3.6\ \mu\text{m}$ (Ashby et al. 2009) and *Herschel* at 250, 350 and 500 microns. We find that the two signals are correlated but the cross-correlation coefficient is weak at 30% or below. Such a weak cross-correlation argues for the scenario that *Spitzer* and *Herschel* are mostly tracing two different populations. To interpret the data, we model the auto and cross-correlation signals using a three component halo model composed of far infrared (FIR) galaxies, intra-halo light (IHL), and faint galaxies.

The paper is structured as follows. In Section 2, we discuss the data analysis and power spectra measurements. This includes the map making process for the *Herschel* and *Spitzer* data using HIPE and Self-Calibration, respectively. This section also explains the mask generation procedure, defines the cross-correlation power spectrum, and discusses sources of error. In Section 3, we describe the halo model including components for FIR galaxies, IHL, and faint galaxies and the MCMC process used to fit the data. Finally, in Sections 4 and 5 we present the results of our model fit, discuss their implications, and give our concluding thoughts.

2. DATA ANALYSIS AND POWER SPECTRA MEASUREMENTS

We discuss the analysis pipeline we implemented for the cross-correlation of *Herschel* and *Spitzer* fluctuations. The study is done in the Boötes field making use of the *Herschel*/SPIRE instrument data taken as part of the *Herschel* Multi-tiered Extragalactic Survey (HerMES; Oliver et al. 2012) and *Spitzer*/IRAC imaging data taken as part of the *Spitzer* Deep Wide Field Survey (SDWFS) (Ashby et al. 2009). We describe the datasets, map-making, source masking and power spectrum measurement details in the sub-sections below.

2.1. Map Making

2.1.1. Far-IR maps with *Herschel*

We make use of the publicly available SPIRE instrument data of the Boötes field taken as part of HerMES from the ESA *Herschel* Science Data Archive². Our map-making pipeline makes use of the Level 1 time-ordered scans that have been corrected for cosmic rays, temperature drifts, and bolometer time response as part of the standard data reduction by ESA. In those timelines we

remove a baseline polynomial in a scan-by-scan basis to normalize gain variations. The SPIRE maps are generated using the *Herschel* Interactive Processing Environment (HIPE) (Ott 2010). For this work we make use of the MADmap (Cantalupo et al. 2010) algorithm that is native to HIPE. It is a maximum likelihood estimate and follows the approach used in Thacker et al. (2013). We do not use the map-maker that was developed for anisotropy power spectrum measurement in (Amblard et al. 2010) due to improvements that have been made to the HIPE and its built-in map-makers since the Amblard et al. study in 2010.

The end products of the map-making process are single tile maps covering roughly 8 square degrees and containing two sets of 80 scans in orthogonal directions with a pixel scale of 6 arcseconds per pixel in all SPIRE bands ($250\ \mu\text{m}$, $350\ \mu\text{m}$, and $500\ \mu\text{m}$). These maps, using publicly available data from HerMES, are generated at a pixel scale one third of the beam size consistent with our previous work as well. Such a sampling allows the point source fluxes to be measured more accurately with an adequate sampling of the PSF. For this study, we are forced to compromise between an accurate sampling of the PSF, point source detection and flux density measurement to get an accurate combination of *Herschel* and *Spitzer* data. Since the native scale of *Spitzer* maps are at 1.2 arcseconds/pixel, we do not want to increase the SPIRE pixel scale substantially. We will return to this issue more below when we discuss our point source masks that were applied to the maps to remove detected sources.

2.1.2. *Spitzer*

The SDWFS (Ashby et al. 2009) maps of the Boötes field consist of four observations taken over 7 to 10 days from 2004 to 2008³. For this analysis we limit our data to the $3.6\ \mu\text{m}$ channel. With four sets of data taken at different roll angles we can ensure our fluctuation measurements are robust to detector systematics. In addition, since the measurements were taken in different years and months, multiple jack-knife tests enable us to reduce and quantify the error from astrophysical systematics such as the zodiacal light (ZL).

To further control the errors and to obtain a uniform background measurement across a very wide area the maps are mosaiced using a SELF-CALIBRATION algorithm (Arendt et al. 2000). The algorithm is able to match the sky background levels with free gain parameters between adjacent overlapping frames using a least squares fitting technique. We make use of the cleaned basic calibrated data (cBCDs) publicly available from the *Spitzer* data archive for the map-making process. These frames have asteroid trails, hot pixels, and other artifacts removed. Our original maps are made at a pixel scale of 1.2 arcsecond per pixel. Unlike our previous work (Cooray et al. 2012), we have repixelized the maps to a 6 arcsecond per pixel scale to match with the pixel scale of our *Herschel* maps.

The *Spitzer* maps span an area of about $10\ \text{deg}^2$, larger than the *Herschel*/SPIRE coverage at $8\ \text{deg}^2$. For this study we extract the overlapping area in both *Spitzer*

² Observation Id's listed in acknowledgements

³ <http://sha.ipac.caltech.edu/applications/Spitzer/SHA/>
Program number GO40839 (PI. D. Stern)

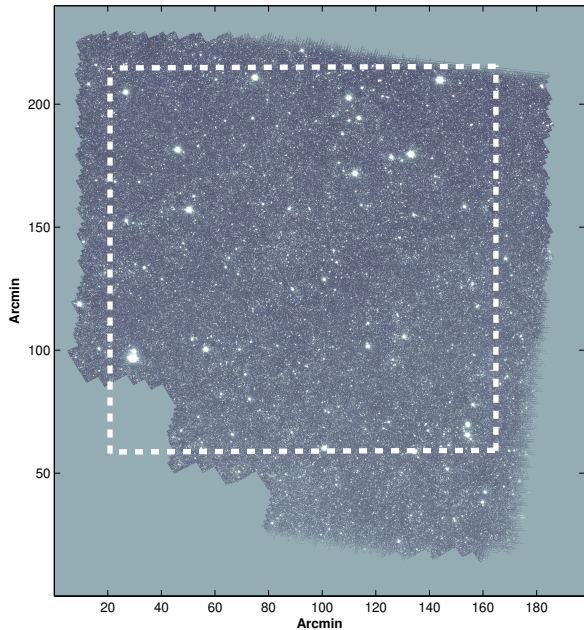


FIG. 1.— *Spitzer* 3.6 μ m Boötes field with only the overlapping area with *Herschel*. The white dashed lines show the cropped region used for the cross-correlation study. We crop to a rectangle to minimize the edge effects and biases from the non-uniform turnaround data in the *Herschel*/SPIRE scan pattern. This region is also selected to maximize the unmasked area.

and *Herschel* as outlined in Figure 1.

2.1.3. Astrometry

To ensure both *Herschel* and *Spitzer* images are registered to the same astrometric frame, we first checked for any offset in the *Spitzer* astrometry against the public catalog of SDWFS sources and corrected the astrometry using GAIA. We then made *Herschel* maps to the same astrometry as *Spitzer*. As a test on our overall astrometric calibration we used Source Extractor (SEXTRACTOR) (Bertin & Arnouts 1996) to detect all sources in both the *Spitzer* and *Herschel* images. We then matched the sources in the two catalogs within a radius of 18 arcseconds (corresponding to the FWHM of the beam in 250 μ m). Next, we took these matches and subtracted their RA and DEC such that a perfect match would have a Δ RA and Δ DEC of zero. Fig. 3 shows a scatter plot of these values in pixels rather than RA and DEC. Perfectly aligned images would show a scatter centered at zero with equal spread in both directions. Our analysis shows a slight offset that is less than a pixel and within our tolerance as the effect on the cross-correlation is negligible since an offset less than a pixel will get binned to the nearest pixel and thus produces no offset.

2.2. Detected Source Masking

We remove the detected sources from our maps so the cross-correlation is aimed at the unresolved fluctuations in both sets of data. We first generate two masks, one for the *Spitzer* data and one for the *Herschel* data (in all three bands). We combine these two masks to a common

mask. This guarantees that both sets of data are free of as much foreground contamination as possible, minimizing spurious correlations by having a masked area in one map that is unmasked in the other. With a common mask we are also able to better handle for mode-coupling effects which masking introduces. The final combined mask (a zoomed in portion can be seen in Fig. 2) removes 61.4% of the pixels.

2.2.1. *Spitzer*

Since our model is based on sources below the detection threshold, we must pay particular attention to generating a relatively deep mask for *Spitzer*. Otherwise unmasked *Spitzer* sources will correlate with the faint *Herschel* sources leading to a cross-correlation; in fact, as we find later, a significant fraction of the cross-correlation is due to faint *Spitzer* sources correlating with *Herschel* sources that are responsible for the SPIRE confusion noise.

We produce the *Spitzer* mask using a combination of catalogs from the NOAO Deep Wide Field Survey (NDWFS) in the B_w , R and I bands, and SEXTRACTOR) catalog that was generated for *Spitzer* maps at a 3-sigma detection threshold. As detailed in our previous work (Cooray et al. 2012), we start by iteratively running SEXTRACTOR with the same parameters used to generate the SDWFS catalogs (Ashby et al. 2009). This catalog is then combined with the NDWFS catalogs in the bands listed above. Like with the *Herschel* mask, we apply a flux cut, remove all pixels 5-sigma from the mean, and convolve everything with the PSF. Finally, we combine this mask with the *Herschel* mask.

Since this image has been rebinned to a larger pixel size by a factor of five at 6 arcsec from our previous work at 1.2 arcsec in Cooray et al. (2012), significant blending occurs from nearby galaxies that are resolved in the 1.2 arcsec pixelized image. One effect of this is to increase the power at high- ℓ by increasing the shot-noise associated with unmasked galaxies. An aggressive mask for *Spitzer*, consistent with Cooray et al. (2012), cannot be used for this study since that will lead to a small fraction of unmasked pixels for the cross-correlation study with *Herschel*. Our main limitation here is not the depth of *Spitzer* imaging data, but the large PSF of *Herschel* maps. In Fig. 4 we compare the power spectrum from Cooray et al. (2012) and the new power spectrum of *Spitzer* imaging data with a mask that retains more of the faint sources.

2.2.2. *Herschel*

In the *Herschel* data, the mask is generated by a simple three step process in each of the SPIRE bands. They are then combined into a single mask. The zeroth step is to crop the region in which *Herschel* and *Spitzer* overlap into a rectangular area as shown in Fig. 1. First, we apply a flux cut at 50 mJy/beam, removing the brightest galaxies and staying consistent with our previous work on the clustering of fluctuations in the SPIRE bands (Amblard et al. 2011; Thacker et al. 2013). Next, to include the extended nature of the sources, we expand the mask by convolving with the point spread function (PSF). Finally, we remove pixels with no data, which arises mostly in 350 μ m and 500 μ m due to the enforced 6 arcsec pixel size (oversampling the PSF), and pixels

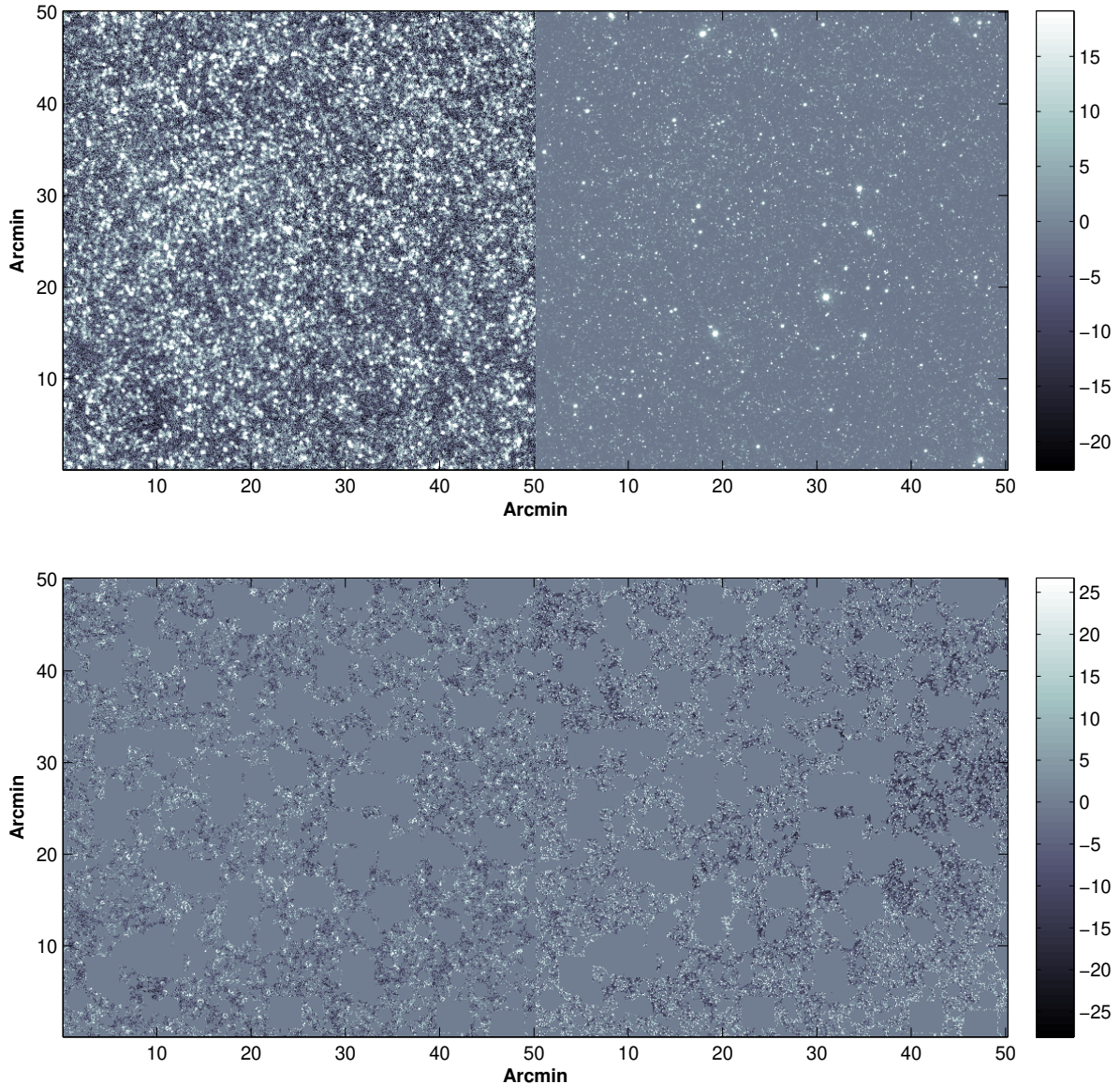


FIG. 2.— A zoomed in image, roughly 0.7 square degrees, of *Herschel* 250 μm (left image) and *Spitzer* 3.6 μm (right image) data of the Boötes/SDWFS field. The upper images are the unmasked maps showing all sources, while the lower images have the mask applied to remove bright detected sources from the cross-correlation study. The mask over the whole area removes 61.4% of the pixels leaving the remainder for the study presented here.

with corrupt data by applying a 5-sigma clip to the images.

The final mask for this study is obtained by multiplying the individual *Herschel* and *Spitzer* masks for the union between the two maps. The auto power spectra we show in Fig. 5 use this combined mask between the two sets of data. A comparison of the shot-noise levels at high- ℓ for the *Herschel* power spectrum with models for source counts reveals that our final mask has an effective depth in the flux density cut at 250 μm of 29.5 mJy/beam. Fig. 5 shows the differences in the auto power spectra with our combined mask vs. power spectra measured with a mask based on a flux density cut for sources at 50 mJy.

2.3. Angular Power Spectra and Sources of Error

Our power spectra and cross power spectra measurements follow the procedures we have used for past work (Thacker et al. 2013; Cooray et al. 2012). Here we summarize the key ingredients related to the uncertainties of the power spectrum measurements.

2.3.1. Instrumental Noise

One benefit of a cross-correlation is that instrumental noise is minimized, especially between two different detectors or imaging experiments. The maps can be thought of as signal, S , plus a noise component, N . So in a cross-correlation we have $M_1 \times M_2 = (S_1 + N_1) \times (S_2 + N_2)$. Since the noise is expected to be random and because these are two different detectors,

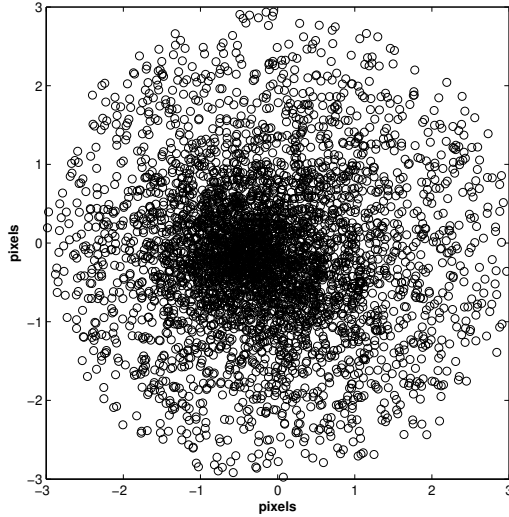


FIG. 3.— Using SEXTRACTOR on all of the maps (the example here shows pairs from $250\mu\text{m}$ and $3.6\mu\text{m}$) we generate a list of detected sources. All of the sources within a radius of 18 arcseconds of each map are identified to be counterparts of each other. For each counterpart we show the offset in their locations in *Herschel* and *Spitzer* maps where we have converted differences in RA and Dec to pixels. Plotted here is the ΔX and ΔY (in pixels) between 4252 sources selected from either *Herschel* or *Spitzer* with a detected counterpart in the other map.

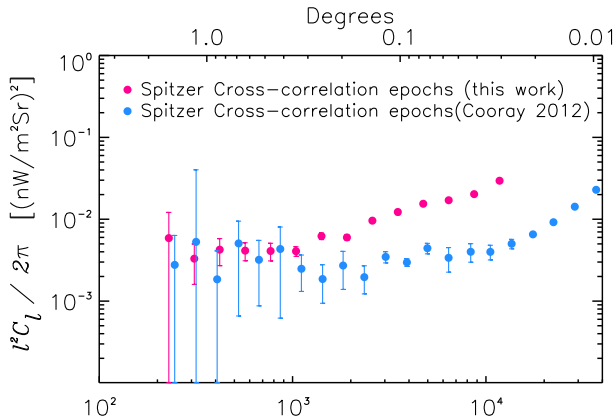


FIG. 4.— Comparison of *Spitzer* power spectra measured in the Boötes field between the current and previous work (Cooray et al. 2012). In the previous work the power spectra measured is the cross-correlation of epochs at 1.2 arcsec/pixel. In this work, however, we have repixelized the maps to 6 arcsec/pixel and created a new mask, which we are not able to make as deep, or else we would end up with no data.

the noise should be uncorrelated, thus dropping out of the cross-correlation.

To get a handle on the instrumental noise component and an estimate of systematic errors like zodiacal light or cirrus contamination, we perform jackknife tests. These tests involve taking half maps for *Herschel* and single epoch maps for *Spitzer* and cross-correlating their differences. For example in *Spitzer* we would take epochs (1 – 2) cross correlated with epochs (3 – 4), where 1 to

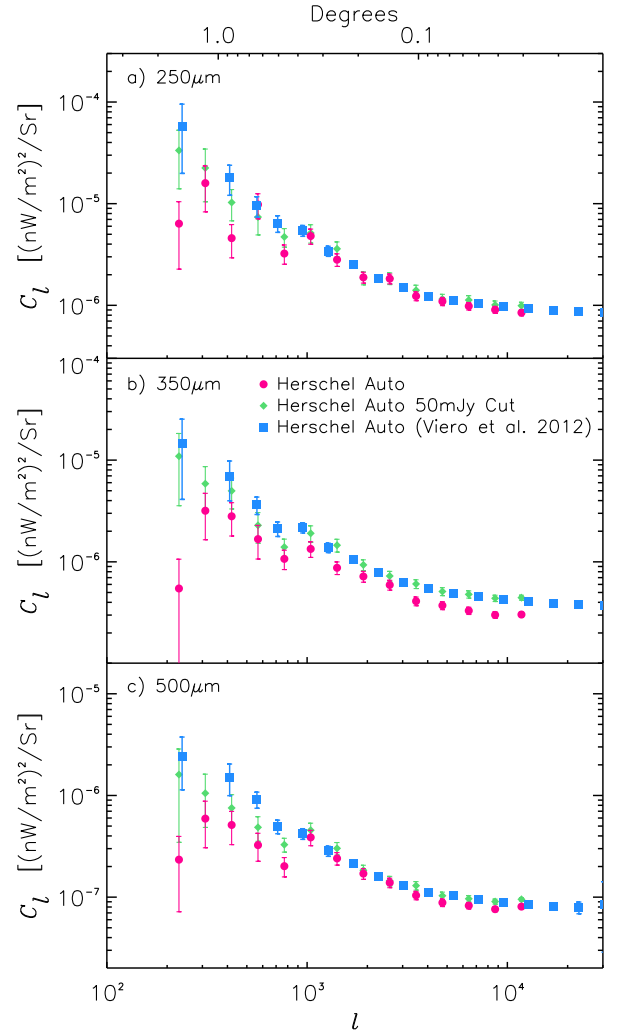


FIG. 5.— The comparison of *Herschel* auto-correlation power spectrum from our map (red points with a mask that removes 61.4% of the pixels) to the measurement in Viero et al. (2013) (blue points). The latter is based on a source mask that removes SPIRE sources brighter than 50 mJy. As discussed in Section 2.2.2 our effective flux density cut is at 29.5 mJy. In addition and just for comparison we also plot the auto-spectrum with a 50mJy/Beam flux cut in green.

4 are the four epochs of the SWDFS survey. We average all combinations of this and find it is stationary about zero. Finally, the variance arising from this is an estimate of the residual noise and is added to the total error budget of the *Spitzer* auto power spectrum.

While it is assumed that the detector noise components of *Herschel* and *Spitzer* do not correlate, we still need to place a limit on any residual noise correlations in the cross-correlation. This is accomplished by taking null tests where we cross-correlate a *Herschel* map with all combinations of epoch differenced maps of *Spitzer*. The variance of this multi epoch cross-correlations are added to our error budget of the *Herschel* and *Spitzer* cross-correlation power spectrum.

2.3.2. Beam Correction

At high ℓ there is a substantial drop in power due to the finite resolution of the detector and this drop in power

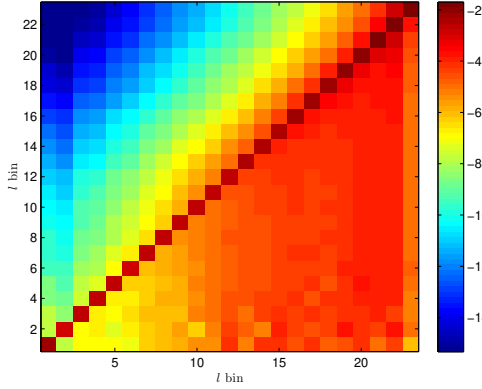


FIG. 6.— Mode-coupling matrix $M_{ll'}$ for the combined mask (log scale).

needs to be accounted for. This is corrected by taking the power spectrum of the PSF (point spread function) and normalizing to be one at low ℓ . For cross spectra we need a correction for the two separate beams. For that we simply use the geometric mean of the two beams. For the *Herschel* data we use the beam calculated by Amblard et al. (2011) based on observations of Neptune. The *Spitzer* beam used was calculated in Cooray et al. (2012) directly from the PSF as described there.

2.3.3. Mode-Coupling Correction

Unlike the case of CMB, infrared background power spectra involves aggressive masks that remove a substantial fraction of the pixels. A consequence of such masking is breaking up larger Fourier modes into smaller modes. This results in a shift of power from low- ℓ to high- ℓ . Using the method from Cooray et al. (2012) we generate a mode-coupling matrix, $M_{\ell\ell'}$, shown in Fig. 6 by making maps of pure tones, masking them, and taking the power spectrum. Thus, by construction the matrix transforms unmasked power to masked power and we simply invert the matrix to obtain a transformation to an unbiased power spectrum.

2.3.4. Map Making Transfer Function

Unfortunately the map making process does not result in a perfect representation of the sky. The map making process can induce fictitious correlations or suppress them based on deficiencies in the scan pattern, the technique that was used to process the timeline data including any filtering that was applied. We capture all of the modifications associated with the map making process by the transfer function, $T(l)$.

For *Herschel* data we calculate the transfer function by making 100 Gaussian random maps and reading them into timeline data using the same pointing information as the actual data. Then we produce artificial maps from these timelines and take the average of the power spectra of each of these maps to the power spectrum in each of the input maps. For the *Spitzer* data, we follow a similar approach but instead of reading data into timelines we create small tiles that are re-mosaiced using the same self-calibration algorithm as the actual data. These simulated tiles include Gaussian fluctuations and instrumental noise consistent with the corresponding tile in the

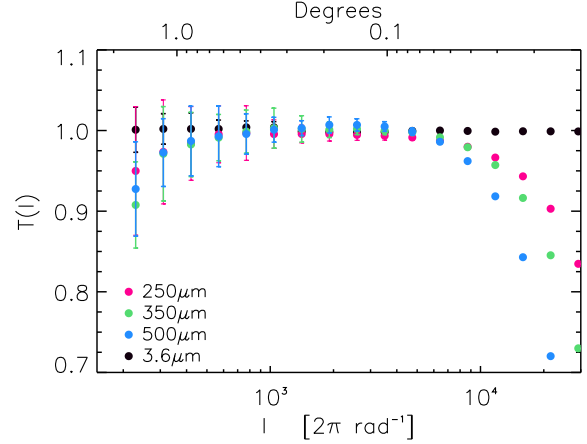


FIG. 7.— Map-making transfer function $T(l)$ for the *Herschel* and *Spitzer* Boötes field anisotropy power spectrum. The uncertainties in the transfer function are calculated from 100 gaussian realizations of the sky as described in Section 2.3.4.

actual data. Due to the dithering and tiling pattern that was used for actual observations in SDWFS with *Spitzer*, the map-making transfer function is essentially one at all angular scales of interest. This is substantially different for *Herschel*/SPIRE with a transfer function that departs from one at low and high ℓ as shown in Fig. 7. The difference at high ℓ is due to the scan pattern that leaves stripes in the data; the difference at low ℓ or large angular scales is due to the filtering that was applied to timeline data to remove gain drifts during an individual scan. That is the process used to make maps and to ensure the map-making process has not generated a bias in the power spectrum.

2.3.5. Power Spectrum Estimate

To put these corrections to use, we must first define the cross-correlation. Given two maps H and S , the cross-correlation is calculated as:

$$\langle C_{li} \rangle = \frac{\sum_{l_1}^{l_2} w(l_x, l_y) \tilde{H}(l_x, l_y) \tilde{S}^*(l_x, l_y)}{\sum_{l_1}^{l_2} w(l_x, l_y)}, \quad (1)$$

where \tilde{H} and \tilde{S} are the 2D Fourier transforms of their respective maps and $w(l_x, l_y)$ is the mask in Fourier space. The auto-spectra follows from the case when $H = S$.

Finally, the final cross power spectrum estimate is obtained from the measured power spectrum, $\tilde{C}_{\ell'}$, with the above described corrections as:

$$C_{\ell} = \frac{M_{\ell\ell'}^{-1} \tilde{C}_{\ell'}}{T_{\ell'} b_{\ell'}^S b_{\ell'}^H}. \quad (2)$$

To generate the *Spitzer* auto-spectrum (Fig 4) we take the average of the permutations of different cross-correlations involving the four epochs of SDWFS. For example, we calculate $(1+2) \times (3+4)$ averaged with all other permutations where 1 to 4 are the four epochs. When compared to our previous work *Spitzer* auto-spectrum deviates at high ℓ . The higher shot-noise is because we

have repixelized the image from 1.2 arcsec/pixel in our prior work to 6 arcsec/pixel here. This also leads to a more shallow mask than our previous work.

Figure 8 shows the cross-correlations with the best-fit model (described below) shown for comparison. Again, we make use of the four different *Spitzer* epochs in the cross-correlation. The cross-correlation is calculated as the average of $(\text{epoch}_i + \text{epoch}_j)/2 \times \text{Herschel}$ where $i \neq j$.

In addition to the instrumental noise term and errors coming from the uncertainties in the beam function and map-making transfer function, we also account for the cosmic variance in our total error budget. More details are available in the Appendix C.

3. HALO MODEL

In this Section, we outline our model for the cross-correlation. The underlying model involves three key components: far-IR galaxies, intra-halo light, and near-IR galaxies.

3.1. Model for FIR background fluctuations from star-forming dusty galaxies

We make use of the conditional luminosity function (CLF) models to calculate the power spectrum of FIR galaxies (Lee et al. 2009; De Bernardis & Cooray 2012). The probability density of a halo/subhalo with mass M to host a galaxy observed in a FIR band with luminosity L (i.e. L_{250} , L_{350} and L_{500} in this work) is given by

$$P(L|M) = \frac{1}{\sqrt{2\pi}\ln(10)L\Sigma} \exp\left\{-\frac{\log_{10}[L/\bar{L}(M,z)]^2}{2\Sigma^2}\right\}, \quad (3)$$

where $\Sigma = 0.3$ Lee et al. (2009) is the variance of $\log_{10}\bar{L}(M,z)$, and $\bar{L}(M,z)$ is the mean luminosity given a halo/subhalo mass M at redshift z which takes the form

$$\bar{L}(M,z) = \bar{L}(M)(1+z)^p F_\nu[\nu_{\text{obs}}(1+z)], \quad (4)$$

where we have

$$\bar{L}(M) = L_0 \left(\frac{M}{M_0}\right)^\alpha \exp\left[-\left(\frac{M}{M_0}\right)^\beta\right]. \quad (5)$$

Here we take $M_0 = 10^{12} M_\odot$ consistent with previous work (Lee et al. 2009; Cooray et al. 2012), L_0 , α and β as free parameters to be fitted by the data⁴. We also consider the redshift evolution of $\bar{L}(M)$ with a factor $(1+z)^p$, where p is a free parameter. The F_ν is spectral energy distribution (SED) for FIR galaxies, which takes into account the fact that the observed frequency ν_{obs} comes from the frequency $\nu = \nu_{\text{obs}}(1+z)$ at z . The SED can be expressed in terms of a modified blackbody normalized at 250 μm

$$F_\nu = \frac{(1 - e^{-\tau})B(\nu, T_d)}{(1 - e^{-\tau_0})B(\nu_0, T_d)}, \quad (6)$$

where $B(\nu, T_d)$ is the blackbody spectrum, T_d is the dust temperature of FIR galaxies, ν_0 is the frequency

⁴ We set $\beta = 0$ when we perform the fitting process since we find β is close to zero as a free parameter (De Bernardis & Cooray 2012).

of 250 μm , $\tau = (\nu/\nu_0)^{\beta_d}$, $\tau_0 = \tau(\nu_0)$ and β_d is the dust emissivity spectral index. We fix $T_d = 35$ K and $\beta_d = 2$ in this work which are consistent with results from observations (Shang et al. 2011; Hwang et al. 2010; Chapman & Wardle 2006; Dunne et al. 2000; Amblard et al. 2010).

Then the luminosity function (LF) can be obtained by

$$\Phi(L,z)dL = dL \int dM P(L|M)n(M,z), \quad (7)$$

where $n(M,z) = n_h(M,z) + n_s(M,z)$ is the total halo mass function, and n_h and n_s are halo and subhalo mass function respectively. In this work, we find that subhalos are not important and cannot affect our results, so we ignore all subhalo terms in our analysis for simplicity, and we have $n(M,z) \simeq n_h(M,z)$. Next, we can estimate the mean comoving emissivity of FIR galaxies, $\bar{j}_\nu(z)$, at frequency ν and redshift z

$$\bar{j}_\nu(z) = \frac{1}{4\pi} \int \Phi(L,z)LdL. \quad (8)$$

Also, we can construct the halo occupation distribution (HOD) with the probability density shown by equation (3). Given a luminosity limit L_{min} determined by a survey, the average number of central galaxies hosted by halos of mass M is

$$\langle N_c(M) \rangle_{L \geq L_{\text{min}}} = \int_{L_{\text{min}}} P(L|M)dL. \quad (9)$$

The 1-halo and 2-halo terms of 3-D power spectrum for FIR galaxies are given by

$$P_{\text{gg}}^{\text{1h}}(k,z) = \int dM n(M,z) \frac{\langle N_g(N_g - 1) \rangle}{\bar{n}_g^2} u^p(k|M,z), \quad (10)$$

$$P_{\text{gg}}^{\text{2h}}(k,z) = \left[\int dM b(M,z) n(M,z) \frac{\langle N_g \rangle}{\bar{n}_g} u(k|M,z) \right]^2 \times P_{\text{lin}}(k,z), \quad (11)$$

where $u(k|M,z)$ is the Fourier transform of the Navarro-Frenk-White (NFW) halo density profile for halos of mass M at redshift z (Navarro et al. 1997), and the power index p takes $p = 1$ when $\langle N_g(N_g - 1) \rangle \leq 1$ and $p = 2$ otherwise (Cooray & Sheth 2002). $b(M,z)$ is the halo bias (Sheth & Tormen 1999), and P_{lin} is the linear matter power spectrum. The \bar{n}_g is the galaxy mean number density which is expressed as

$$\bar{n}_g(z) = \int dM n(M,z) \langle N_g(M) \rangle. \quad (12)$$

Here $\langle N_g(M) \rangle$ is the mean number of galaxies hosted by a halo of mass M . Since we ignore the subhalo term in this work, we assume $\langle N_g(M) \rangle \simeq \langle N_c(M) \rangle$ and $\langle N_g(N_g - 1) \rangle \simeq \langle N_c(M) \rangle^2$, which is a good approximation in our calculation.

The 2-D angular cross-power spectrum of FIR galaxies at observed frequencies ν and ν' can be obtained with the help of Limber approximation as

$$C_{\ell,\text{FIR}}^{\nu\nu'} = \int dz \left(\frac{d\chi}{dz} \right) \left(\frac{a}{\chi} \right)^2 \bar{j}_\nu(z) \bar{j}_{\nu'}(z) P_{\text{gg}}(k,z), \quad (13)$$

where χ is the comoving distance, a is the scale factor, $\bar{j}_\nu(z)$ is the mean emissivity shown in equation (8), and

$P_{\text{gg}}(k, z) = P_{\text{gg}}^{1\text{h}}(k, z) + P_{\text{gg}}^{2\text{h}}(k, z)$ is the galaxy power spectrum where $k = \ell/\chi$.

3.2. Intra-Halo Light

According to Cooray et al. (2012), intra-halo light (IHL) mean luminosity for halos with mass M at redshift z is assumed to be

$$\bar{L}_{\text{IHL}}(M, z) = f_{\text{IHL}}(M) L^{2.2}(M) (1+z)^{p_{\text{IHL}}} F_{\lambda}^{\text{IHL}}, \quad (14)$$

where $f_{\text{IHL}}(M)$ is the IHL fraction of the total halo luminosity, which has the form

$$f_{\text{IHL}}(M) = A_{\text{IHL}} \left(\frac{M}{M_0} \right)^{\alpha_{\text{IHL}}}. \quad (15)$$

Here A_{IHL} is an amplitude factor and α_{IHL} is a mass power index fixed to be 0.1 (Cooray et al. 2012). $L^{2.2}(M) = L_0^{2.2}(M)/\lambda_0$ is the total halo luminosity at $2.2 \mu\text{m}$, where $\lambda_0 = 2.2 \mu\text{m}$ and $L_0^{2.2}(M)$ is given by (Lin et al., 2004)

$$L_0^{2.2}(M) = 5.64 \times 10^{12} h_{70}^{-2} \left(\frac{M}{2.7 \times 10^{14} h_{70}^{-1} M_{\odot}} \right)^{0.72} L_{\odot}. \quad (16)$$

Then we can scale the total luminosity at $2.2 \mu\text{m}$ to the other wavelengths by the IHL SED F_{λ}^{IHL} . Here the IHL SED is assumed to be the SED of old elliptical galaxies which are composed of old and red stars (Krick & Bernstein 2007), and we normalize $F_{\lambda}^{\text{IHL}} = 1$ at $2.2 \mu\text{m}$.

The 1-halo and 2-halo terms of the 2-D IHL angular cross-power spectrum at observed wavelengths λ and λ' can be estimated by

$$C_{\ell, \text{IHL}}^{\lambda\lambda', 1\text{h}} = \frac{1}{(4\pi)^2} \int dz \left(\frac{d\chi}{dz} \right) \left(\frac{a}{\chi} \right)^2 \times \int dM n(M, z) u^2(k|M, z) \bar{L}_{\text{IHL}}^{\lambda} \bar{L}_{\text{IHL}}^{\lambda'}, \quad (17)$$

$$C_{\ell, \text{IHL}}^{\lambda\lambda', 2\text{h}} = \frac{1}{(4\pi)^2} \int dz \left(\frac{d\chi}{dz} \right) \left(\frac{a}{\chi} \right)^2 P_{\text{lin}}(k, z) \times \int dM b(M, z) n(M, z) u(k|M, z) \bar{L}_{\text{IHL}}^{\lambda} \times \int dM b(M, z) n(M, z) u(k|M, z) \bar{L}_{\text{IHL}}^{\lambda'}. \quad (18)$$

The total 2-D IHL angular cross-power spectrum is then given by

$$C_{\ell, \text{IHL}}^{\lambda\lambda'} = C_{\ell, \text{IHL}}^{\lambda\lambda', 1\text{h}} + C_{\ell, \text{IHL}}^{\lambda\lambda', 2\text{h}}. \quad (19)$$

3.3. Model for NIR background fluctuations from known galaxy populations

We follow Helgason et al. (2012) to estimate the NIR background fluctuations from known galaxy populations. We make use of their empirical fitting formulae of luminosity functions (LFs) for measured galaxies in UV, optical and NIR bands out to $z \sim 5$. Then, we estimate the mean emissivity $\bar{j}_{\nu}(z)$ at the rest-frame frequencies and redshift to the observed frequency. We adopt the HOD model to calculate the 3-D galaxy power spectrum

using equation (10) and (11) with $\langle N_{\text{g}} \rangle = \langle N_{\text{c}} \rangle + \langle N_{\text{s}} \rangle$ and $\langle N_{\text{g}}(N_{\text{g}} - 1) \rangle \simeq 2\langle N_{\text{s}} \rangle \langle N_{\text{c}} \rangle + \langle N_{\text{s}} \rangle^2$, where

$$\langle N_{\text{c}} \rangle = \frac{1}{2} \left[1 + \text{erf} \left(\frac{\log_{10} M - \log_{10} M_{\text{min}}}{\sigma_M} \right) \right], \quad (20)$$

and

$$\langle N_{\text{s}} \rangle = \frac{1}{2} \left[1 + \text{erf} \left(\frac{\log_{10} M - \log_{10} 2M_{\text{min}}}{\sigma_M} \right) \right] \left(\frac{M}{M_{\text{s}}} \right)^{\alpha_{\text{s}}}. \quad (21)$$

Here M_{min} denotes the mass that a halo has 50% probability of hosting a central galaxy, and σ_M is the transition width. We assume the satellite term has a cutoff mass with twice the mass of central galaxy and grows as a power law with slope α_{s} and normalized by M_{s} . We set $M_{\text{min}} = 10^9 M_{\odot}$, $\sigma_M = 0.2$, $M_{\text{s}} = 5 \times 10^{10} M_{\odot}$, and $\alpha_{\text{s}} = 1$ (Helgason et al. 2012). The 2-D angular cross-power spectrum $C_{\ell, \text{NIR}}^{\nu\nu'}$ can be calculated by equation (13) with $\bar{j}_{\nu}(z)$ and $P_{\text{gg}}(k, z)$ of unresolved galaxies.

3.4. Model Comparison

In this work, we have three angular auto power spectra C_{ℓ}^{Her} in the far-infrared from *Herschel*/SPIRE at 250, 350 and 500 μm , one angular auto power spectrum C_{ℓ}^{Spi} from *Spitzer* at 3.6 μm , and three cross-power spectra C_{ℓ}^{cross} between *Herschel* and *Spitzer* data. Using the models discussed in the previous Sections, we fit all these auto and cross power spectra with a single model.

As mentioned, we consider three components in our model to fit each dataset. For C_{ℓ}^{Her} , we have $C_{\ell}^{\text{Her}} = C_{\ell}^{\text{FIR}} + C_{\ell, \text{shot}}^{\text{Her}}$, where $C_{\ell}^{\text{FIR}} = C_{\ell, \text{FIR}}^{\nu\nu'}$, $\nu_{\text{obs}}, \nu'_{\text{obs}}$ are the observed frequencies at 250, 350 or 500 μm , and $C_{\ell, \text{shot}}^{\text{Her}}$ is the shot-noise term. In a similar way, for C_{ℓ}^{Spi} , we take $C_{\ell}^{\text{Spi}} = C_{\ell}^{\text{NIR}} + C_{\ell}^{\text{IHL}} + C_{\ell, \text{shot}}^{\text{Spi}}$ at 3.6 μm . For C_{ℓ}^{cross} , it is expressed as $C_{\ell}^{\text{cross}} = C_{\ell}^{\text{FIR} \times \text{NIR}} + C_{\ell}^{\text{FIR} \times \text{IHL}}$. The model details of these cross powerspectra are outlined in the Appendix.

Since the shot-noise is a constant and dominant at high ℓ , we derive the shot-noise terms from the data at the high ℓ and fix them in the fitting process. The values of the shot-noise terms we find are $C_{\ell, \text{shot}}^{\text{Her}} = 8.4 \times 10^{-7}, 3.0 \times 10^{-7}$ and $8.0 \times 10^{-8} \text{ nW}^2 \text{m}^{-4} \text{sr}^{-1}$, and $C_{\ell, \text{shot}}^{\text{cross}} = 1.7 \times 10^{-8}, 3.0 \times 10^{-9}$ and $1.4 \times 10^{-9} \text{ nW}^2 \text{m}^{-4} \text{sr}^{-1}$ at 250, 350 and 500 μm , respectively. For $C_{\ell, \text{shot}}^{\text{Spi}}$, we scale the shot-noise of NIR background $C_{\ell, \text{shot}}^{\text{NIR}}$ given by equation (13) in Helgason et al. (2012) to match the high- ℓ data of *Spitzer* at 3.6 μm . This is done by adjust the minimum apparent magnitude m_{min} , and we find $m_{\text{min}} = 23$ which gives $C_{\ell, \text{shot}}^{\text{NIR}} = 3.1 \times 10^{-10} \text{ nW}^2 \text{m}^{-4} \text{sr}^{-1}$.

We employ the Markov Chain Monte Carlo (MCMC) method to perform the fitting process. The Metropolis-Hastings algorithm is adopted to determine the probability of accepting a new MCMC chain point (Metropolis et al. 1953). We use χ^2 distribution to calculate the likelihood function $\mathcal{L} \propto \exp(-\chi_{\text{tot}}^2/2)$. For the three datasets, we have $\chi_{\text{tot}}^2 = \chi_{\text{Her}}^2 + \chi_{\text{Spi}}^2 + \chi_{\text{cross}}^2$, and

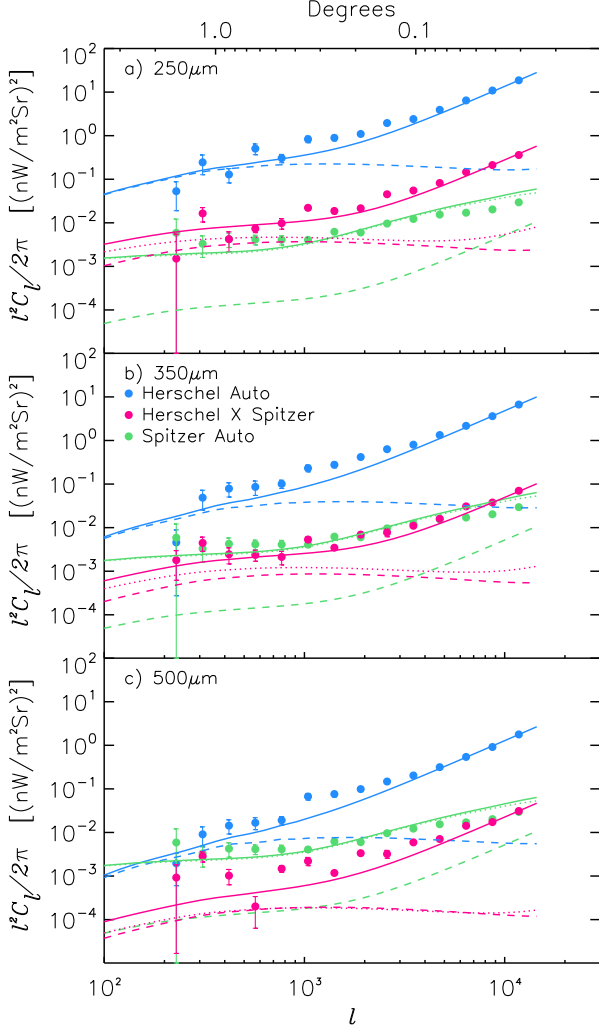


FIG. 8.— The auto and cross angular power spectra of *Herschel* (at 250, 350 and 500 μm) and *Spitzer* (at 3.6 μm) surveys. The blue solid and dashed lines are the total fitting results and FIR galaxy power spectra, respectively. The green solid, dotted, and dashed are the fittings for the total, IHL and NIR galaxy power spectra. The pink solid line is the total cross-power spectrum fit while the dotted and dashed correspond to far-IR cross IHL and far-IR cross near-IR respectively.

the χ^2 is given by

$$\chi^2 = \sum_{i=1}^{N_d} \frac{(C_\ell^{\text{obs}} - C_\ell^{\text{th}})^2}{\sigma_\ell^2}, \quad (22)$$

where N_d is the number of the data points, C_ℓ^{obs} and C_ℓ^{th} are the angular power spectra from observation and theory, and σ_ℓ is the error for each data point.

For simplicity we take $z_{\min} = 0$, $z_{\max} = 6$, $M_{\min} = 10^9 h^{-1} M_\odot$ and $M_{\max} = 10^{14} h^{-1} M_\odot$ when we calculate the integral over redshift and halo mass in the power spectra. We use a uniform prior probability distribution for the free parameters in our model. The parameters and their ranges are as follow: $\log_{10} L_0 \in (-9, 1)$, $\alpha \in (-5, 5)$, $p \in (0, 5)$ for the FIR galaxy model, and $A_{\text{IHL}} \in (-5, 0)$, $p_{\text{IHL}} \in (-5, 5)$ for the IHL model. We generate twelve parallel MCMC chains for each dataset,

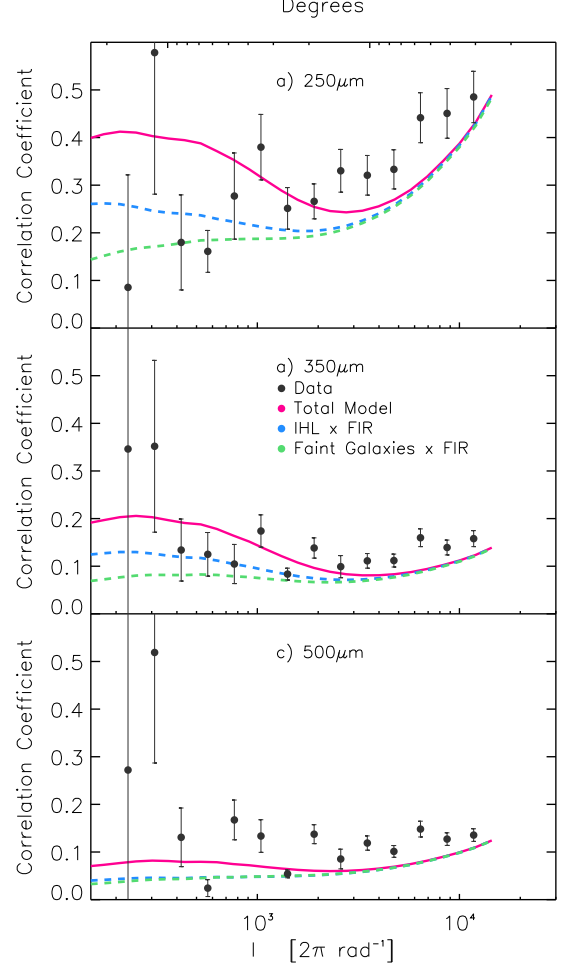


FIG. 9.— Correlation coefficient for the cross-correlation of *Herschel* and *Spitzer* (250, 350, 500 μm \times 3.6 μm). The pink line corresponds to the total best fit halo model. The blue and green dashed lines show the component breakdown of the total halo model into the two terms that make up the total cross correlation. The blue line results from the correlation between IHL and FIR while the green line is from faint galaxies in the NIR correlated with FIR.

and collect about 120,000 chain points after the chains reach convergence. After the burn-in process and thinning the chains, we merge all the chains together and get about 10,000 chain points to illustrate the probability distribution of the free parameters. The details of our MCMC method can be found in Gong & Chen (2007).

4. RESULTS AND DISCUSSION

In this Section, we discuss the results from the data analysis and the MCMC model fits to the auto and cross power spectrum data. We will then outline estimates of derived quantities from the model fitting results, such as the redshift distribution of the far and near-IR intensity and the cosmic dust density.

4.1. Power spectra

In Figure 8, we show the angular auto and cross-power spectra of *Herschel* and *Spitzer* in the Boötes field. The top, middle and bottom panels are for *Herschel* 250, 350 and 500 μm , respectively. The blue solid curve is total best-fit power spectrum for *Herschel* power spectrum,

TABLE 1
THE BEST-FIT VALUES AND 1σ ERRORS OF THE MODEL
PARAMETERS FROM THE MCMC CONSTRAINTS.

	250 μm	350 μm	500 μm
$\log_{10} L_0$	-6.5 ± 0.5	-7.0 ± 0.5	-7.9 ± 1.1
α	0.23 ± 0.06	0.24 ± 0.08	0.22 ± 0.11
p	3.9 ± 0.12	3.9 ± 0.20	3.9 ± 0.25
$\log_{10} A_{\text{IHL}}$	-1.70 ± 0.04	-1.75 ± 0.04	-1.74 ± 0.04
p_{IHL}	-3.2 ± 0.4	-2.5 ± 0.3	-2.6 ± 0.3

which is comprised of two components, i.e. FIR galaxies (blue dashed), and total shot-noise (not shown). Similarly, the green solid line is the best-fit for *Spitzer* auto power spectrum, which has contributions given by IHL (green dotted) and NIR faint galaxies (green dashed). As described in Cooray et al. (2012) the shot-noise of *Spitzer* power spectrum can be described by the faint galaxies, though the clustering of such galaxies fall short of the fluctuations power spectrum at tens of arcminute angular scales. The red solid line is the total cross correlation, including a shot-noise term not shown here, while the red dotted and dashed lines separate the cross-correlation to the main terms given by IHL correlating with faint far-IR dusty galaxies and faint near-IR galaxies correlating with faint far-IR dusty galaxies, respectively. In terms of the cross-correlations we find that these two terms are roughly comparable.

Another comparison of the data and model is shown in Fig. 9. Here, we calculate the correlation coefficient separately from the data and compare to the correlation coefficient of the best-fit model. Displaying the information in this way is a valuable check of the relative strength of correlation. As the far-IR wavelength is increased from 250 μm to 500 μm we find a less of a correlation between *Herschel* and *Spitzer*. Not only does the total correlation decrease, from our model fit we also find that the correlation between IHL and dusty far-IR galaxies, as a fraction of the total correlation, is also decreased.

The best-fit values and 1σ errors of the model parameters are shown in Table 1. We find the MCMC forces just a shot-noise term, i.e. a straight line, to fit the data if we use data points out to $\ell \sim 10^5$ because the errors at high ℓ (small scales) are very small compared to the errors at large scales. For these reasons, our results are obtained by fitting to the power spectrum data at $\ell < 10^4$, and ignoring all data points at $\ell > 10^4$ in the fitting process.

4.2. Intensity redshift distribution

Using the fitting results of the best-fit model parameters and their errors, we estimate the redshift distribution of $d(\nu I_\nu)/dz$ for far-IR dusty galaxies in the three SPIRE bands as

$$\frac{d(\nu I_\nu^{\text{FIR}})}{dz} = \frac{c}{H(z)(1+z)^2} \nu \bar{j}_\nu(z), \quad (23)$$

where c is the speed of light, $H(z)$ is the Hubble parameter, and $\bar{j}_\nu(z)$ is the mean emissivity given by equation (8). Also, the redshift distribution of $d(\nu I_\nu)/dz$ for the IHL component can be obtained by

$$\frac{d(\nu I_\nu^{\text{IHL}})}{dz} = \frac{c}{4\pi H(z)(1+z)^2} \int dM n(M, z) \bar{L}_{\text{IHL}}, \quad (24)$$

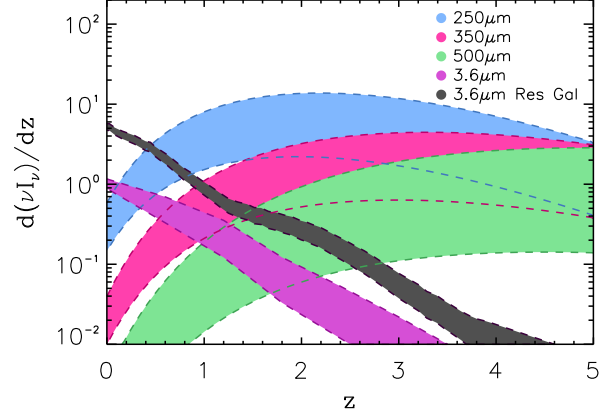


FIG. 10.— Redshift distribution of $d(\nu I_\nu)/dz$ for *Herschel* FIR galaxies at 250, 350 and 500 μm , and *Spitzer* IHL and residual galaxies at 3.6 μm .

where $\bar{L}_{\text{IHL}}(M, z)$ is the mean IHL luminosity given by equation (14), and $n(M, z)$ is the halo mass function.

In Figure 10, we show $d(\nu I_\nu)/dz$ as a function of the redshift for *Herschel* galaxies at 250, 350 and 500 μm , and *Spitzer* IHL and faint unresolved galaxies at 3.6 μm . We find the redshift distribution has a turnover between $z = 1$ and 2 for 250 μm , which indicates the intensity is dominated by the sources at $z = 1 \sim 2$ for 250 μm . For 350 μm , the turnover of $d(\nu I_\nu)/dz$ is not obvious and is shifted to higher redshift around $z = 3$. For 500 μm , we find that the sources at $z > 3$ dominate the intensity. The increase in redshift with the wavelength for dusty sources we find here is consistent with the well-known result in the literature (Bethemini et al. 2011; Amblard et al. 2011; Viero et al. 2013). On the other hand, the $d(\nu I_\nu)/dz$ of *Spitzer* IHL and residual galaxies at 3.6 μm has their maximum values at $z = 0$ and decreases quickly with increasing redshift. This shape, which is substantially different from *Herschel* dusty galaxies, is the main reason that the cross-correlation signal between *Herschel* and *Spitzer* is below 0.5 at 250 μm with a decrease to a value below 0.2 at 500 μm . The decrease with increasing wavelength is consistent with the overall model description. If naively interpreted, the small cross-correlation with *Herschel* could have been argued as evidence for a very high-redshift origin for the *Spitzer* fluctuations, similar to the arguments that have been for the origin of *Spitzer*-Chandra cross-correlation (Cappelluti et al. 2012). Our modeling suggest the opposite: *Spitzer* fluctuations are very likely to be dominated by a source at $z < 1$ while intensity fluctuations in *Herschel* originate from $z = 1$ and above at 250, 350 and 500 μm .

4.3. Cosmic Dust Density

As an application of our models we also derive the fractional cosmic dust density Ω_{dust} of galaxies from the fitting results. Following Thacker et al. (2013), the Ω_{dust} for galaxies is given by

$$\Omega_{\text{dust}}(z) = \frac{1}{\rho_0} \int dL \Phi(L, z) M_{\text{dust}}(L), \quad (25)$$

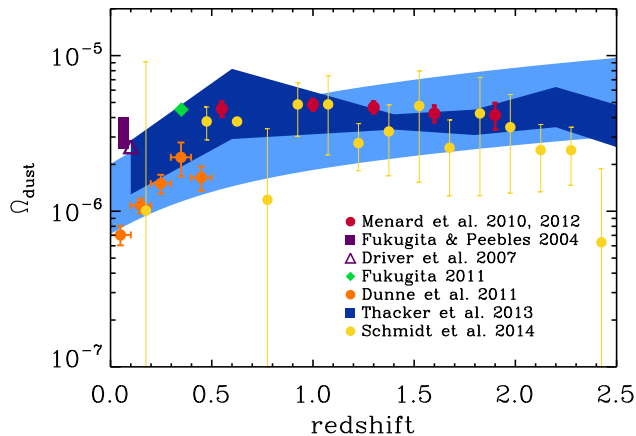


FIG. 11.— The fractional cosmic dust density Ω_{dust} as a function of redshift from FIR galaxies. The light blue shaded region shows the 1σ range of Ω_{dust} for FIR galaxies derived from our MCMC fitting results in this paper. We also show the results from different observations for Ω_{dust} . The orange squares are the measurement of H-ATLAS dust mass function in Dunne et al. (2010), and the other data are based on the extinction measurements of the SDSS and 2dF surveys (Menard et al. 2010; Menard & Fukugita 2012; Fukugita & Peebles 2004; Fukugita et al. 2011; Driver et al. 2007). We also include recent measurements from Schmidt et al. (2014) using the cross-correlation between the Planck High Frequency Instrument and quasars from the Sloan Digital Sky Survey DR7. Finally, we include results from Thacker et al. (2013) as the dark blue shaded region.

where ρ_0 is the current cosmic critical density, $\Phi(L, z)$ is the luminosity function, and M_{dust} is the dust mass with IR luminosity L with temperature assumed to be $35K$ that we fix in the power spectrum model. We make use of equation (4) of Fu et al. (2012) to estimate M_{dust} from IR luminosity (Thacker et al. 2013). Also, we assume the dust opacity κ_d takes the form as $\kappa_d = A_\kappa \nu^{\beta_d}$, where $\beta_d = 2$ is the dust emissivity spectral index, and A_κ is the normalization factor which is estimated by $\kappa_d = 0.07 \pm 0.02 \text{ m}^2 \text{ kg}^{-1}$ at $850 \mu\text{m}$ (Dunne et al. 2000; James et al. 2002).

We show Ω_{dust} as a function of redshift in Figure 11. The blue shaded region is the 1σ range of the Ω_{dust} from the FIR. We also show the other measurements for comparison. The orange squares are from the H-ATLAS dust mass function as measured in Dunne et al. (2010), and the other data are

based on the extinction measurements of the SDSS and 2dF surveys (Menard et al. 2010; Menard & Fukugita 2012; Fukugita & Peebles 2004; Fukugita et al. 2011; Driver et al. 2007). We find our Ω_{dust} result from galaxies is consistent with the other measurements, which has Ω_{dust} increasing at higher redshift.

5. SUMMARY

We have calculated the cross-correlation power spectrum of the cosmic infrared background at far and near-IR wavelengths using *Herschel* and *Spitzer* in the Boötes field. We measured the correlation coefficient to be between 10-40% with the highest correlation seen in the $250 \mu\text{m}$ band and the lowest in $500 \mu\text{m}$.

Recent results from Cooray et al. (2012) and Zemcov et al. (2014) suggest that the near-IR background anisotropies have a mostly low redshift origin at $z < 1$, arising from intra-halo light and faint dwarf galaxies. Meanwhile the far-IR signal is dominated by dusty galaxies peaking at a redshift of ~ 1 and above (Amblard et al. 2010; Thacker et al. 2013; Viero et al. 2013). By cross correlating *Herschel* with *Spitzer* we are able to provide a check on the robustness of such a model. We find that not only can such a model fit the auto-correlations they were designed to fit, but can also explain the cross-correlation signal, including the wavelength dependence of the cross-correlation coefficient.

This work was supported by NSF AST-1313319 and GAANN at UCI. The public *Herschel* data in the *Herschel* Science Archive was taken by HerMES with observation Id's 1342187711 to 1342187713, 1342188090, 1342188650 to 1342188651, 1342188681 to 1342188682, and 1342189108. HIPE was a joint development by the *Herschel* Science Ground Segment Consortium, consisting of ESA, the NASA *Herschel* Science Center, and the HIFI, PACS and SPIRE consortia. We thank Rick Arendt for sharing of his self-calibration pipeline for *Spitzer* data. We thank ESA for maintaining the *Herschel* Science Archive and for making available reduced and calibrated time-ordered data of every SPIRE scan that was done during the *Herschel* mission.

APPENDIX

CROSS POWER SPECTRA

Here we discuss the 2-D angular cross-power spectra of *Herschel* and *Spitzer* in our model. The total cross-power spectrum C_ℓ^{cross} is composed of four components which are

$$C_\ell^{\text{cross}} = C_\ell^{\text{FIR} \times \text{NIR}} + C_\ell^{\text{FIR} \times \text{IHL}}. \quad (\text{A1})$$

Here $C_\ell = \nu_{\text{obs}} \nu'_{\text{obs}} C_\ell^{\nu\nu'}$ where ν_{obs} is the observed frequency at $250, 350$ or $500 \mu\text{m}$ of *Herschel* survey, and ν'_{obs} is the observed frequency at $3.6 \mu\text{m}$ of *Spitzer* survey.

The 1-halo and 2-halo terms of $C_{\ell, \text{FIR} \times \text{NIR}}^{\nu\nu'}$ are given by

$$C_{\ell, \text{FIR} \times \text{NIR}}^{\nu\nu', 1h} = \int dz \left(\frac{d\chi}{dz} \right) \left(\frac{a}{\chi} \right)^2 \bar{j}_\nu(z) \bar{j}_{\nu'}(z) \int dM n(M, z) \frac{\sqrt{\langle N_g(N_g - 1) \rangle_\nu} \sqrt{\langle N_g(N_g - 1) \rangle_{\nu'}}}{\bar{n}_g^\nu(z) \bar{n}_g^{\nu'}(z)} \sqrt{u^{p_\nu}} \sqrt{u^{p_{\nu'}}}, \quad (\text{A2})$$

$$C_{\ell, \text{FIR} \times \text{NIR}}^{\nu\nu', 2h} = \int dz \left(\frac{d\chi}{dz} \right) \left(\frac{a}{\chi} \right)^2 \bar{j}_\nu(z) \bar{j}_{\nu'}(z) \left[\int dM b(M, z) n(M, z) \frac{\langle N_g \rangle_\nu}{\bar{n}_g^\nu(z)} u(k|M, z) \right] \\ \times \left[\int dM b(M, z) n(M, z) \frac{\langle N_g \rangle_{\nu'}}{\bar{n}_g^{\nu'}(z)} u(k|M, z) \right] P_{\text{lin}}(k, z). \quad (\text{A3})$$

Here ν and ν' denote FIR and NIR bands for Herschel and *Spitzer* respectively. Then we have $C_{\ell, \text{FIR} \times \text{NIR}}^{\nu\nu'} = C_{\ell, \text{FIR} \times \text{NIR}}^{\nu\nu', 1h} + C_{\ell, \text{FIR} \times \text{NIR}}^{\nu\nu', 2h}$.

The 1-halo and 2-halo terms of $C_{\ell, \text{FIR} \times \text{IHL}}^{\nu\nu'}$ are

$$C_{\ell, \text{FIR} \times \text{IHL}}^{\nu\nu', 1h} = \frac{1}{4\pi} \int dz \left(\frac{d\chi}{dz} \right) \left(\frac{a}{\chi} \right)^2 \bar{j}_\nu(z) \int dM n(M, z) \frac{\sqrt{\langle N_g(N_g - 1) \rangle_\nu}}{\bar{n}_g^\nu(z)} \sqrt{u^{p_\nu}(k|M, z)} \bar{L}_{\text{IHL}}^{\nu'}(M, z) u(k|M, z), \quad (\text{A4})$$

$$C_{\ell, \text{FIR} \times \text{IHL}}^{\nu\nu', 2h} = \frac{1}{4\pi} \int dz \left(\frac{d\chi}{dz} \right) \left(\frac{a}{\chi} \right)^2 \bar{j}_\nu(z) \left[\int dM b(M, z) n(M, z) \frac{\langle N_g \rangle_\nu}{\bar{n}_g^\nu(z)} u(k|M, z) \right] \\ \times \left[\int dM b(M, z) n(M, z) u(k|M, z) \bar{L}_{\text{IHL}}^{\nu'}(M, z) \right] P_{\text{lin}}(k, z). \quad (\text{A5})$$

So we get $C_{\ell, \text{FIR} \times \text{IHL}}^{\nu\nu'} = C_{\ell, \text{FIR} \times \text{IHL}}^{\nu\nu', 1h} + C_{\ell, \text{FIR} \times \text{IHL}}^{\nu\nu', 2h}$.

FLAT SKY APPROXIMATION

Using the formalism of Hivon et al. (2002), we show how to get the flat sky approximation which allows the use of Fourier transforms instead of spherical harmonics to calculate the power spectrum. The flat sky approximation requires $\theta \ll 1$ and $\ell \gg 1$. We start by defining the weighted sum over the multipole moments as

$$M(\vec{\ell}) = \sqrt{\frac{4\pi}{2\ell + 1}} \sum_{m=-\ell}^{\ell} i^{-m} M_{\ell m} e^{im\phi_\ell}. \quad (\text{B1})$$

For this derivation we need the following approximations for when $\theta \ll 1$ and $\ell \gg 1$. The first is known as the Jacobi-Anger expansion of the plane wave,

$$e^{i\vec{\ell} \cdot \vec{r}} = \sum_m i^m J_m(\ell\theta) e^{im(\phi - \phi_\ell)}, \quad (\text{B2})$$

where $J_m(\ell\theta)$ are Bessel functions and we use the fact that since θ is small $r \approx \theta$.

Next, to show that $Y_{\ell m}$ is approximately $\sqrt{\ell/2\pi} J_m(\ell m) e^{im\phi}$, we start with the general Legendre equation and perform a change of variables $\cos(\theta) \Rightarrow \cos(\frac{\theta'}{\ell})$. Using the fact that $\theta'/\ell \ll 1$ to simplify, and multiply the equation by θ'^2/ℓ^2 to get it into the correct form. Now, one can recognize the equation as Bessel's equation with solution $J_m(\theta') = J_m(\ell\theta)$.

Putting this all together, we decompose the maps into spherical harmonics and introduce some simplifications to obtain,

$$M(\hat{n}) = \sum_{m\ell} M_{\ell m} Y_{\ell m}, \quad (\text{B3}) \\ = \sum_{m\ell} M_{\ell m} \sqrt{\frac{\ell}{2\pi}} J_m(\ell m) e^{im\phi}, \\ = \sum_{m\ell} \frac{\ell}{2\pi} \int \frac{d\phi_\ell}{2\pi} M(\vec{\ell}) i^m J_m(\ell m) e^{im(\phi - \phi_\ell)}, \\ \approx \int \frac{d^2\ell}{(2\pi)^2} M(\vec{\ell}) e^{i\vec{\ell} \cdot \vec{r}}.$$

CROSS CORRELATION POWER SPECTRUM AND COSMIC VARIANCE

Analogous to the convolution theorem, correlations obey a similar relation except with a complex conjugate. Below, \mathcal{F} denotes 2D Fourier transforms and \star denotes cross-correlation, where M_i are 2D maps:

$$\mathcal{F}(M_1 \star M_2) = \mathcal{F}(M_1) \cdot \mathcal{F}(M_2)^* . \quad (\text{C1})$$

Since we can use Fourier transforms as a suitable basis to obtain a power spectrum (see B in Appendix), we are guaranteed that the cross-correlation above is also a power spectrum. Putting it together, for a specific ℓ_i bin and including Fourier masking, we obtain

$$\langle C_{\ell_i} \rangle = \frac{\sum_{l_1}^{l_2} w(l_x, l_y) \widetilde{M}_1(l_x, l_y) \widetilde{M}_2^*(l_x, l_y)}{\sum_{l_1}^{l_2} w(l_x, l_y)} . \quad (\text{C2})$$

Here $\widetilde{M}_1 = \mathcal{F}(M_1)$ and $w(l_x, l_y)$ is a Fourier mask that has the value one for modes we keep and zero for modes we mask. The binning is done in annular rings so $l_1 \geq l_x^2 + l_y^2$ and $l_2 \leq l_x^2 + l_y^2$.

Cosmic variance, δC_ℓ , is the expected variance on the power spectrum estimate at each ℓ mode and is given by

$$\delta C_\ell = \sqrt{\frac{2}{f_{\text{sky}}(2\ell+1)\Delta\ell}} (C_\ell^{\text{auto}} + N_\ell), \quad (\text{C3})$$

where N_ℓ is the noise power spectrum generated through jackknife and similar techniques, f_{sky} is the fraction of the sky covered by the map, and $\Delta\ell$ is the width of the ℓ -bin.

For the cross-correlation spectrum the cosmic variance is

$$\delta C_\ell = \sqrt{\frac{1}{f_{\text{sky}}(2\ell+1)\Delta\ell} \left[(C_{A\ell}^{\text{auto}} + N_{A\ell})(C_{B\ell}^{\text{auto}} + N_{B\ell}) + (C_\ell^{A \times B})^2 \right]}, \quad (\text{C4})$$

where $C_\ell^{A \times B}$ is the cross-correlation power spectrum.

REFERENCES

- Amblard, A., Cooray, A., Serra, P., et al. 2010, *A&A*, 518, L9
 Amblard, A., et al. 2011, *Nature*, 470, 510
 Arendt, R. G., Fixsen, D. J., & Moseley, S. H. 2000, *ApJ*, 536, 500
 Ashby, M. L. N., et al. 2009, *ApJ*, 701, 428
 Bertin, E. & Arnouts, S. 1996, *A&AS*, 117, 393
 Bethermin, M., Dole, H., Lagache, G., et al. 2011, *A&A*, 529, A4
 Cantalupo, C. M., et al. 2010, *ApJS*, 187, 212
 Cappelluti, N., Kashlinsky, A., and Arendt, R. G., et al. 2012, *ApJ*, 769, 68
 Chapman, J. F. & Wardle, M. 2006 *MNRAS*, 371, 513
 Carollo, D., et al. 2010, *ApJ*, 712, 692727
 Cooray, A., Sheth, R.K. 2002, *PR*, 372, 1
 Cooray, A., et al. 2012, *Nature*, 490, 514
 Courteau, S., et al. 2011, *ApJ*, 739, 20
 De Bernardis, F., & Cooray, A. 2012, *ApJ*, 760, 14
 Dole, H., Lagache, G., Puget, J.-L., et al. 2006, *A&A*, 451, 417
 Driver, S. P., et al. 2007, *MNRAS*, 379, 1022
 Dunne, L., Eales, S. A., Edmunds, M. G., et al. 2000, *MNRAS*, 315, 115
 Dunne, L., Gomez, H., da Cunha, E. S., et al. 2010, *MNRAS*, 417, 1510
 Fu, H., Jullo, E., Cooray, A., et al. 2012, *ApJ*, 753, 12
 Fukugita, M., Peebles P. J. E., 2004, *ApJ*, 616, 643
 Fukugita, M., 2011, arXiv, arXiv:1103.4191
 Gonzalez, A. H., Zabludoff, A. I. & Zaritsky, D. 2005, *ApJ*, 618, 195-213
 Gong, Y., & Chen, X. 2007, *PRD*, 76, 123007
 Griffin, M. J., Abergel, M. J., Abreu, A., et al. 2010, *A&A*, 518, L3
 Helgason, K., Ricotti, M., & Kashlinsky, A. 2012, *ApJ*, 752, 113
 Hivon, E., et al. 2002, *ApJ*, 567, 2
 Hwang, H.S., Elbaz, D., Magdis, G., et al., 2010, *MNRAS*, 409, 75
 James, A., Dunne, L. et al., 2002 *MNRAS*, 335, 753
 Kashlinsky, A., Arendt, R. G., Mather, J., & Moseley, S. H. 2005, *Nature*, 438, 45
 Kashlinsky, A., Arendt, R. G., Mather, J., & Moseley, S. H. 2007, *ApJL*, 654, L5
 Kashlinsky, A., Arendt, R. G., Ashby, M. L. N., Fazio, G. G., Mather, J., & Moseley S. H. 2012, *ApJ*, 753, 63
 Krick, J. E., & Bernstein, R. A. 2007, *ApJ*, 134, 466-493
 Lee *et al.*, *ApJ* 695, 368 (2009)
 Lin, Y. T., Mohr, J. J., & Stanford, S. A. 2004, *ApJ*, 610, 745-761
 Matsumoto, T., Seo, H. J., Jeong, W.-S., Lee, H. M., Matsuura, S., Matsuhara, H., Oyabu, S., Pyo, J., et al. 2011, *ApJ*, 742, 124
 Menard B., Scranton R., Fukugita M., Richards G., 2010, *MNRAS*, 405, 1025
 Menard, B., & Fukugita, M. 2012, *ApJ*, 754, 116
 Metropolis, N., Rosenbluth, A. W., Rosenbluth, M. N., Teller, A. H., & Teller, E. 1953, *JCP*, 21, 1087
 Navarro, J. F., Frenk, C. S., White, S. D. M. 1997, *ApJ*, 490, 493
 Oliver, S. J., Wang, L., Smith, A. J., Altieri, B., Amblard, A., et al. 2010, *A&A*, 518, L21
 Ott, S. 2010, in *Astronomical Society of the Pacific Conference Series*, Vol. 434, *Astronomical Data Analysis Software and Systems XIX*, ed. Y. Mizumoto, K.-I. Morita, & M. Ohishi, 139
 Pillbratt, G. L., et al. 2010, *A&A*, 518, L1
 Planck Collaboration and Ade, P. A. R., Aghanim, N., Armitage-Caplan, C., Arnaud, M., Ashdown, M., Atrio-Barandela, F., Aumont, J., Baccigalupi, C., Banday, A. J., et al. 2014, *A&A*, 571, A16
 Purcell, C. W., Bullock, J. S. & Zentner, A. R. 2008, *MNRAS*, 391, 550-558
 Schmidt, S., Menard, B., et al., 2014, *MNRAS* 446, 2696
 Shang, C., et al. 2011, arXiv:1109.1522
 Sheth, R. K., Tormen, G. 1999, *MNRAS*, 308, 119
 Thacker, C., Cooray, Smidt, et al. 2013, *ApJ*, 768, 58
 Viero, M. P., Wang, L., Zemcov, M., et al. 2013, *ApJ*, 772, 77
 Yue, B., Ferrara, A., Salvaterra, R., Xu, Y., & Chen, X. 2013, *MNRAS*, 433, 15561566
 Yue, B., Ferrara, A., Salvaterra, R., Xu, Y., & Chen, X. 2014, *MNRAS*, 440, 1263-1273
 Zemcov, M. and Smidt, J. and Arai, T. and Bock, J. and Cooray, A., et al. 2014, *Science*, 346, 732-735